Full Length Article

Experimental setup for Weak Interaction Studies with Radioactive ion-beams WISArD

D. Atanasov [a,*], F. Cresto [b], L. Nies [a,1], M. Pomorski [c,2], M. Versteegen [c], P. Alfaurt [c],
V. Araujo-Escalona [d], P. Ascher [c], B. Blank [c], L. Daudin [c], D. Guillet [c], X. Fléchard [b], J. Ha [d],
A. Husson [c], M. Gerbaux [c], J. Giovinazzo [c], S. Grévy [c], T. Kurtukian-Nieto [c], L. Leterrier [b],
R. Lica [a,e], E. Liénard [b], C. Mihai [e], C. Neacsu [e,f], A. Ortega-Moral [c], G. Pascovici [e], M. Roche [c],
N. Severijns [d], S. Vanlangendonck [d], A. Welker [a], D. Zákoucký [g]

[a] European Organization for Nuclear Research (CERN), Esplanade des Particules 1, CH-1211, Geneva, Switzerland
[b] Université de Caen Normandie, ENSICAEN, CNRS/IN2P3, LPC Caen UMR6534, F-14000, Caen, France
[c] LP2i Bordeaux, UMR5797, Université de Bordeaux, CNRS, F-33170, Gradignan, France
[d] KU Leuven, Instituut voor Kern- en Stralingsfysica, B-3001, Leuven, Belgium
[e] H. Hulubei National Institute for Physics and Nuclear Engineering - IFIN-HH, R-077125, Bucharest, Romania
[f] Physics Department, University Politehnica of Bucharest, R-077125, Bucharest, Romania
[g] Nuclear Physics Institute, Acad. Sci. Czech Rep., CZ-25068, Rez, Czech Republic

ARTICLE INFO

ABSTRACT

The article describes the commissioning and technical development of the Weak Interaction Studies with ^{32}Ar Decay (WISArD) experiment, installed at the radioactive ion-beam facility ISOLDE/CERN. The experiment aims to extend the present limits on scalar and tensor currents in the weak interaction and hence search for physics beyond the Standard Model. The evaluation of these limits relies on measuring the proton energy in beta-delayed proton emission, sensitive to both the beta-neutrino angular correlation coefficient $a_{\beta\nu}$ and the Fierz interference term b. The method tries to improve previous studies by considering the positron-proton coincidences when determining the kinematic shift in the energy of the emitted protons. Using this coincidence technique, the $a_{\beta\nu}$ and b coefficients will be measured at the per mil level. Simulations were employed to optimize the ion beam transport efficiency and validate proof-of-principle results obtained in November 2018 (Nov2018). Upgrades are ongoing, and we are looking into improvements to the overall performance of the setup.

1. Motivation

The Standard Model (SM) of particle physics was essentially confirmed, following the discovery of the Higgs boson. The agreement between experiment and corresponding theoretical predictions has been impressive [1], celebrating its internal consistency. Nevertheless, despite past and present phenomenological success, several remaining aspects need to be addressed to be considered a complete theory: for example, the apparent dark matter content in the Universe, the matter-antimatter asymmetry or the origin of CP violation. At present, experiments at the Large Hadron Collider to produce new mediating bosons of the weak interaction do not seem to indicate direct evidence for *New Physics* [2]. These results have triggered much interest in

the precision frontier because searches for tiny effects in nuclear and neutron beta decay can address the energy scale for the *New Physics*.

The weak interaction, mediating nuclear beta decay and some channels of pion and muon decays, is integrated into the wider framework of the SM with the vector (V) and axial–vector (A) formalism. The experimental evidence for the time-invariant pure $V - A$ form of the SM interaction has been strong for the last 60 years. However, from a more general theoretical point of view, requiring only Lorenz invariance, the presence of scalar (S) or tensor (T) type contributions are not excluded. In super-allowed pure Fermi (F) and pure Gamow-Teller (GT) beta decays, the treatment of the nuclear structure corrections is greatly simplified, allowing one to perform the most stringent tests for the possible presence of the contributions mentioned above [3].

---

* Correspondence to: LP2i Bordeaux, France
E-mail address: dinko.atanasov@cern.ch (D. Atanasov).
[1] Present address: Institute für Physik, Universität Greifswald, 17487 Greifswald, Germany
[2] Present address: Faculty of Physics, University of Warsaw, 02-093 Warszawa, Poland
[3] Note the exclusion of the pseudo-scalar type currents due to their relevance only at relativistic energies.

The weak coupling constants C_i of the different interaction types ($i = V, A, S, T$)[3] can be experimentally determined through the decay transition probability. The general description was established by Jackson, Treiman and Wyld (JTW) in 1957 [4] and the distribution function for an ensemble of non-oriented nuclei is expressed as

$$\omega(E_e, \Omega_e, \Omega_\nu) \propto$$
$$\omega_0(Z, E_e)\left(1 + b\frac{m_e}{E_e} + a_{\beta\nu}\frac{\overline{p_e} \cdot \overline{p_\nu}}{E_e E_\nu}\right) \tag{1}$$

with $\omega_0(Z, E_e)$ containing the phase space factor and the Fermi function; $E_{e,\nu}$ and $p_{e,\nu}$ are the energy and momenta of the β particle and the neutrino, respectively; m_e is the rest mass of the electron, b is the Fierz interference term and $a_{\beta\nu}$ the beta-neutrino correlation coefficient. However, it is difficult to measure both $a_{\beta\nu}$ and b independently and the observable extracted from experiments can be expressed as:

$$\tilde{a} = \frac{a_{\beta\nu}}{(1 + \alpha b)} \tag{2}$$

where the coefficient α is linked to the measured beta energy spectrum, the experimental technique and to the geometry of the setup [5]. This modified correlation coefficient ($\tilde{a}$) provides access to experimental determination of the non-SM contributions. The numerical value predicted by the SM assuming the strict $V - A$ structure of the weak interaction is $a_{\beta\nu} = 1$ for pure Fermi decays and $a_{\beta\nu} = -1/3$ for pure Gamow-Teller decays. The value of the Fierz interference term in both SM transitions is $b = 0$. Thus, any admixtures of S or T currents to the dominant V or A currents, assuming maximal parity violation and no time-reversal symmetry violation of the standard terms, would result in a measurable deviation from the expectation value such that:

$$a_F \approx 1 - \frac{|C_S|^2 + |C_S'|^2}{|C_V|^2}$$
$$b_F \approx \pm Re\left(\frac{C_S + C_S'}{C_V}\right)$$
$$a_{GT} \approx -\frac{1}{3}\left[1 - \frac{|C_T|^2 + |C_T'|^2}{|C_A|^2}\right] \tag{3}$$
$$b_{GT} \approx \pm Re\left(\frac{C_T + C_T'}{C_A}\right)$$

where the $\pm$ sign refers to $\beta^\mp$ decay. The present benchmark for the absolute uncertainties of the correlation coefficients can be found in detail in Ref. [6].

2. Experiment

2.1. Measurement principle

Studies of the $\tilde{a}_{\beta\nu}$ coefficient are possible because the momentum of the neutrino can be inferred from measurements of the momentum of the recoiling daughter nucleus. However, one drawback limiting this type of measurement is the relatively small recoil energy delivered to the daughter nucleus by the emitted leptons (sub-keV scale). Hence, the high-precision experiments performed nowadays aim at reducing possible external systematic factors influencing the final result by using atom or ion traps or other means [7–12]. Alternatively, if the daughter nucleus is unstable to β-delayed particle emission, its momentum can be determined by the kinematics of the decay products [9,13–16]. When a particle is emitted from a moving source (i.e. the recoiling daughter nucleus) its measured energy will be subject to a kinematic shift that reflects the motion of the recoiling daughter nucleus. See, for example, the schematic overview in Fig. 1. Thus, one can study the energy spectrum of subsequently emitted light energetic particles instead of the slow, heavy nuclei whose atomic effects, for example, must be taken into account. The time scale of the particle emission must be short, such that the decay can occur long before the recoiling nucleus

has appreciably slowed down, if the latter is not in a free environment. One can use this technique to simultaneously study multiple beta-decay transitions (F or GT) by determining the kinematic shift for each beta-delayed group.

The kinematic shift will be observed as a line broadening in the energy spectrum of the beta-delayed particles. The broadening effect simply reflects the isotropic emission of particles in the daughter decay affected by the recoil direction. Instead of studying the broadening effect, one could require a specific angular correlation between the beta and the beta-delayed particles (*coincidence*). Using coincidences, a mean energy shift is observed with respect to the *singles* in the energy of the beta-delayed particle. This approach makes the result less dependent on the precise knowledge of the detector response function.

A demonstration of this technique was performed in 2018, where a 5-fold improvement in precision on $\tilde{a}_{\beta\nu}$ was shown to be at reach with the coincidence technique [17]. The detection setup was constructed with readily available particle detectors and focused on the beta-delayed protons emitted in the decay of ^{32}Ar towards the isobaric analogue state (IAS) in ^{32}Cl. The following sections outline the setup used in this experiment and its upgrades to reach the per-mil level (0.1%). Experiments at this level of precision can probe gauge bosons related to new physics with masses of the order of 5 to 10 TeV [6,18].

2.2. Setup overview

The setup, which will apply the kinematic shift technique, is prepared at the radioactive ion-beam (RIB) facility ISOLDE/CERN [19,20], within the scope of the Weak Interaction Studies with 32-Argon Decay (WISArD) collaboration. The RIBs delivered by the facility ensure studies of the angular correlation coefficient of a wide variety of β-decay transitions. In the first phase of the experimental campaign, the isotope of interest is ^{32}Ar. The argon isotope is produced at ISOLDE in a spallation reaction after a primary proton beam driven by the Proton Synchroton Booster of CERN at an energy of 1.4 GeV impinges onto nano-CaO target material [21]. Next, the argon atoms diffuse out from the hot target container ($\sim$750 °C) to the Versatile Discharge Ion Source (VADIS/VD7) [22], where an ion-beam is produced. After extraction and acceleration to a kinetic energy of 30 keV, the ion-beam is sent for isobaric mass selection (A/Q) through the ISOLDE high-resolution mass separator.

A significant part of the WISArD ion-beam transport system reuses the existing infrastructure of its ancestor experiment — WITCH [23]. The WISArD beamline, thus, follows the previously established logical separation that is, namely, horizontal (HBL), vertical (VBL), solenoid magnet (SBL) and ion-source (IBL) beam lines. However, the current implementation differs from WITCH by its mode of operation, considering the ion-beam manipulations and data collection. For example, the ion-beam in the past was accumulated, cooled and bunched in the upstream Penning trap system of ISOLDE-REXTRAP [24]. With the new implementation, the trap will operate in transmission mode, and thus the ion-beam will be continuous.

2.3. Ion-source beam line (IBL)

The primary purpose of the IBL sector, shown in Fig. 2 is to provide a stable ion beam with an energy of 30 keV and intensity of up to a few nA to commission the electrostatic elements in the rest of the setup. The design of the source closely follows the one of REXTRAP. It consists of a base flange holding the ionizing unit, a conical graphite cylinder filled with zeolite material, an extraction electrode and an extraction lens.
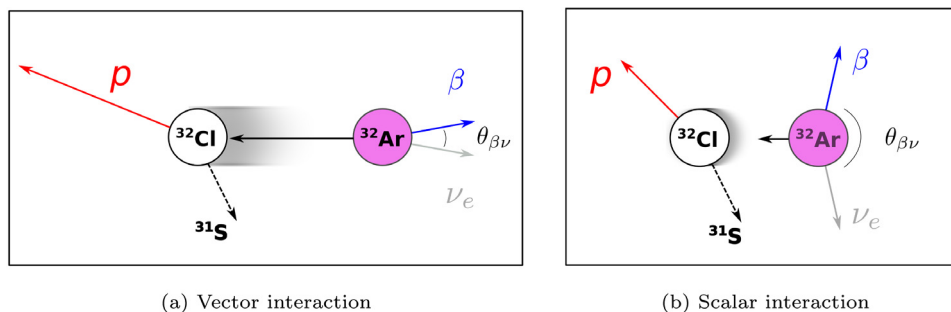
(a) Vector interaction

(b) Scalar interaction

Fig. 1. Schematic representation of the decay kinematics of a pure Fermi transition and its influence on the beta-delayed proton energy. In panel (a) the maximum emission probability occurs at $\theta_{\beta\nu} = 0°$ corresponding to the dominant Vector interaction, while in panel (b) for a Scalar interaction it occurs close to $\theta_{\beta\nu} = 180°$.
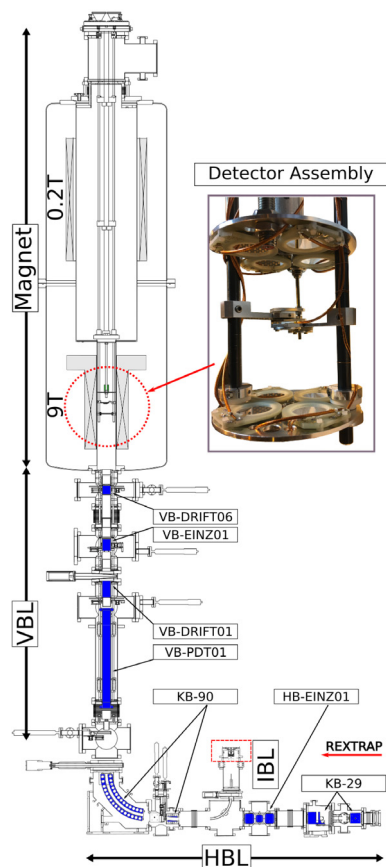

Fig. 2. Schematic drawing of the WISArD beamline. The total height of the setup is about 7 m. The inset picture shows the detector assembly as used in the Proof-of-Principle experiment. Further details are given in the text.

2.4. Horizontal beamline (HBL)

The horizontal beamline, shown in Fig. 2, consists of several electrostatic components, and its primary purpose is to transport the RIBs from the entrance of the apparatus towards the subsequent sections. These components form two kicker-bender assemblies (KB-29 and KB-90 in Fig. 2) and a high-voltage Einzel lens (HB-EINZ01). The electrostatic kickers consist of two parallel deflection plates with an area of 60×60 mm^2 and a gap of 30 mm. Both plates are tilted over an angle of 3.75° with respect to the beam axis, thus, acting as a trajectory switch deflecting ions towards the bender electrodes. The bender assembly consists of two spherical electrodes, of 385 mm radius for the inner one and of 415 mm radius for the outer one. The HB-EINZ01 is placed between the entrance and exit of both kicker-bender assemblies and

has a classical 3-electrode structure. It ensures optimal beam quality over the range of roughly 2.5 m in the HBL. The two outer electrodes are set to ground potential, while the central electrode is adjusted to high-voltage, typically around 12 kV for an ion-beam energy of 30 keV. Steerer plates are also present in the HBL, allowing additional fine corrections of the ion-beam trajectories.

2.5. Vertical beamline (VBL)

The vertical beamline, shown in Fig. 2, comprises ten stainless steel, cylindrically shaped electrodes with an internal diameter of 60 mm. The primary use of the electrodes is to focus and inject the beam into the magnet region. At four locations, doublets of X-Y steerer plates are installed, allowing to correct for possible shifts in the ion-beam trajectory. The first part of VBL comprises a 780 mm long cylindrical electrode. In the past, this electrode was used as a Pulsed Drift Tube (VB-PDT01), adjusting the original ion-beam kinetic energy (30–60 keV) to 1.5 keV. In the WISArD implementation, the ion-beam is not slowed down, and hence the VB-PDT01 is only used as a regular drift region. The electrode design of the second part of the VBL is split into several shorter segments, providing flexibility during ion-beam manipulation. Notably, the second to last electrode ((VB-DRIF06)) is actively used as an Einzel lens, forcing ion trajectories parallel to the magnetic field lines generated by the superconducting magnet in the downstream section.

2.6. Magnet section

The last section of the WISArD beamline is a superconducting magnet system manufactured by Oxford Instruments (see Fig. 2) and capable of producing magnetic fields up to 9 T. The magnet has two primary coil windings designed to produce a homogeneous magnetic field at two locations — the first one with a maximum strength of 9 T and the second one of 0.2 T. The weaker field coil is not used in the context of the setup described here, but note that the initial shimming of the magnet was done assuming both coils being operated. Further details of the magnetic profile field and homogeneity will be given in Section 3.2. The 9 T magnet surrounds a cylindrical vacuum tube with a 130 mm diameter and 482 mm height. Access to that volume is only possible through an opening at the very top of the cryostat system — some 2.5 m away. The inner walls of the cryostat vessel (magnet's bore) are physically connected to the magnet's cryogenic system (liquid nitrogen shield) and hence are cooled down to approximately -30 ℃.

2.7. Detection setup - DSet2018

The proof-of-principle detection system hereafter called DSet2018 consists of four aluminium rods, that extend to the center of the 9 T volume. Two of the rods are fixed to carry the load of the detectors, while the other two constrain the assembly and can rotate. Other components are coupled to the tower, most notably the two disks and a
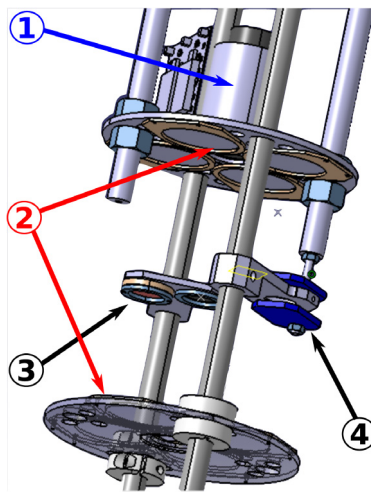
Fig. 3. CAD drawing of the DSet2018 detectors system. See text for more details.

Table 1
Estimates of the total transport efficiency for the Nov2018 experiment in comparison with the values obtained from SIMION simulations for ideal transport. Additionally, the expected improvements after the upgrade of the VBL sector are shown.

Sector	Transmission (%)		
	Nov2018	Nov2018*	Upg2021*
REX-WIS	98	–	–
HBL	75	90	90
VBL	16	22	95
Total	12	19	>84

The columns with ∗ indicate the SIMION simulations.

mount. The former supported both the beta and proton detectors, while the latter allows the insertion of either the ion-beam diagnostics or the implantation foil. The detector's assembly, shown in Fig. 3, used in the DSet2018 experiment comprises the following components:

1. A scintillation detector of a *polystyrene* base produced by ENVINET for the SuperNEMO project [25] was used for the beta particle detection. It was designed with an optimal ratio of concentrations of the activator (pTP) 1.5% and the wavelengthshifter (POPOP) 0.005% [26]. The dimensions of the detector were 20 mm in diameter and 50 mm in length. It was wrapped with a layer of teflon and a light-tight tape. A Silicon photomultiplier type Hamamatsu S13360-6050PE was coupled with optical grease to the scintillator for scintillation photon detection.
2. Eight 300 μm thick silicon detectors used to detect the beta-delayed protons, their active area being 30 mm in diameter.
3. A catcher foil, used to implant the radioactive argon beam made of a 6 μm thick aluminized Mylar foil with a diameter of 20 mm. A Faraday cup used to monitor the intensity of the implanted beam.
4. ^{208}Po alpha source with 300 Bq activity. The source is double sided and allowed calibration of detectors in both hemispheres simultaneously. The quoted activity is per side. When not in use it was placed in its *parking* position between two 2 mm thick aluminium plates.

The catcher foil was mounted on a metallic frame placed at the center of the magnetic field. Four proton detectors (Si1U to Si4U) were placed at a distance of 65.5 mm above the catcher plane. The rest (Si1D to Si4D) were mounted in a mirrored configuration below the catcher. The beta detector was positioned in the upper hemisphere of the detection assembly. The argon beam, coming from a direction below the catcher, passed through an opening of 20 mm in the lower detector support. Note that this is a major bottleneck for the implanted intensity as it requires good handling of the transported ion beam while ions are moving in the gradient of the magnetic field.

2.8. Outcome of Nov2018 and main limitations

The results obtained in the Nov2018 experiment [17] were in agreement with the SM predictions for both F and GT transitions, with a precision of about 4% being reached despite the short beam time and the rudimentary setup used. As discussed in Sec. VI of Ref. [17], several limitations have been identified which one must overcome in

order to reduce the statistical and systematic uncertainty of a future measurement. Factors related to reducing the statistical errors are beam transmission and production, detection solid angle, and a higher energy resolution for the proton detectors. Factors related to the systematic errors include detector dead layer thickness and homogeneity, source and detector relative positions, magnetic field homogeneity, and positron backscattering (on catcher foil and beta detector surface). In the following sections we present the upgrades undertaken to reduce or study these uncertainties.

3. WISArD upgrades

3.1. Ion-beam transport and optimization

The evaluation of the transport efficiencies and the beam shape was made with the SIMION ion and electron optics simulation workbench [27]. The entire set of electrostatic elements of the WISArD beamline were split into four parts, following the general division of the actual apparatus. The goal of the optimization procedure was to maximize the ion-beam intensity at the catcher plane while preserving the ion-beam characteristics. The final parameters obtained in each section were used as starting parameters to optimize the downstream one. Optimal voltages were found through an iterative procedure. A first rough Monte-Carlo-like parameter search constrained the initial parameter space, followed by a more localized simplex downhill optimizer to further refine the optima [28]. Note that steerer elements along the setup were not included in these simulations. During the Nov2018, good transport was achieved up to the entrance of VBL (see Table 1). The transport in the VBL itself was limited by a lack of focusing electrodes and high-voltage power supplies (limited to +4 kV). A maximum transport efficiency of about 12% was achieved during the experiment. To further improve the ion-beam transport, simulations were extended to utilize higher voltages on the various electrodes in the VBL. A crucial step is located at the position of the fringe field of the superconducting magnet. The field lines of the magnet curve away from the beam axis and create an up to 0.5 T strong radial component for off-axis particles, which inevitably leads to a severe broadening of the beam. The effect on the beam profile at the catcher plane compared to the previous settings is shown in Fig. 4. One can see that only a fraction of the beam is guided through the opening in the support plate of the lower detectors. The effect is reduced by focusing the beam before entering the fringe field region. Power supplies with V_{max} = +20 kV are needed to address this effect. Using this new larger parameter space as input for the simulations, a new set of optimal transport settings was identified where total transmission of >84% can be reached.

3.2. Magnetic field profile

The magnetic field profile was determined in a series of measurements conducted to examine the systematic uncertainty estimated in Nov2018. The measurements are based on a translating fluxmeter adapted from Ref. [29]. Furthermore, we investigated the influence on the homogeneity of the 9 T coil without operating the 0.2 T coil and
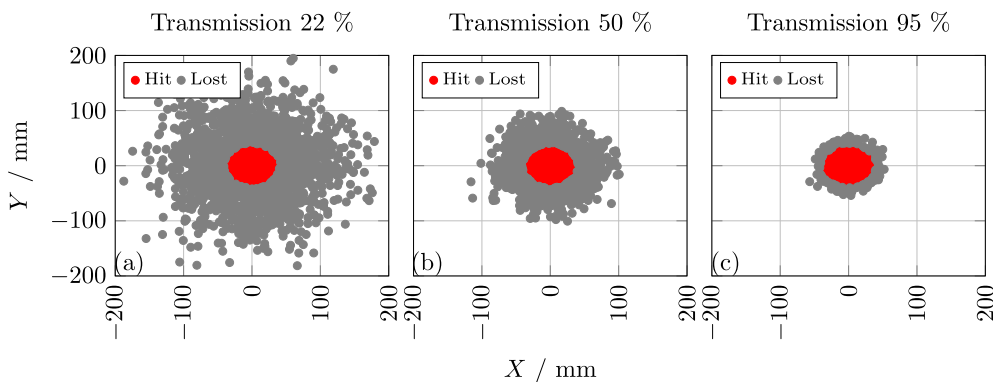
Fig. 4. Simulated beam transmission through the vertical beam line using SIMION. Beam direction is inward and perpendicular to the X-Y plane. Ions hitting the catcher foil are shown in red (Hit), while those hitting the disk (Lost) are shown in gray. Panel (a) represents settings used during the Nov2018 experiment, i.e. no electrostatic electrodes employed, (b) settings with only two electrodes, and (c) optimal settings using 4 electrodes, namely VB-PDT01, VB-DRIF01, VB-EINZ01, VB-DRIF06 in Fig. 2.

validated the initial shimming done in 2001. The fluxmeter is designed explicitly for solenoid magnets and consists of (a) a round coils array on a Printed Circuit Board (PCB), (b) a wire draw encoder, (c) a carbon-profile shaft, and (d) Fast Digital Integrators (FDIs) electronics for measurement. The PCB comprises five concentric disks with a specific diameter (D_i = 10, 28, 48, 68 and 88 mm) and 16 quadrant arcs mounted on a slider, traveling inside an anti-cryostat (vacuum vessel isolating the cold bore wall from the ambient environment). The slider is made of teflon, a non-conducting and non-magnetic material. The encoder had a resolution of 0.014 mm over the 3 m travel range, while it was mounted at the top surface of the anti-cryostat. The slider is then mounted to the shaft, placed vertically and hooked up to the in-situ hoist. A single measurement involves moving the fluxmeter back and forth in the available travel range (almost the total length of the magnet's bore) while the FDIs acquire the signals at 500 kHz from the induction coils. At least three complete travels were made per magnetic field strength. The field profile for the operating strength of the magnet is shown in Fig. 5. One can thus evaluate the variations in the axial and radial magnetic field strength at 4 T in a range of ±100 mm around the center plane. The relative variation of the axial magnetic field is at the level of $\Delta B_z(D_i)/B_z \approx 5.10^{-5}$, while the radial field homogeneity is at the level of $\Delta B_r \approx 1.10^{-3}$ mT (not shown). Note that it was not possible to assess the absolute field level, with a relative accuracy better than 10^{-3}. Measurements were performed at a steady state and ramping-up and ramping-down the current in the primary coil. The results for all magnetic field strengths are in perfect agreement with the information provided by the manufacturer. According to the previous study performed for the DSet2018 configuration, systematic uncertainties due to magnetic field are expected to be below the 10^{-4} level for $\tilde{a}$.

3.3. Tailor-made silicon detectors

New silicon detectors were designed and manufactured specifically for WISArD. These detectors will improve two key areas: solid angle coverage and energy resolution. The resolution of this setup is expected to be less than 10 keV (FWHM) for protons of energy around 3.3 MeV, which will be a factor of 4 better with respect to the DSet2018 detectors. The new detectors are 300 μm-thick single-sided strip detectors manufactured by Micron [30]. The front face of the detectors comprises 5 strips with a strip layout designed to have a constant capacitance of approximately 100 pF per strip, providing a similar preamplifier response for each strip (see Fig. 6). The detectors have a trapezoidal shape so that when combined, they form a truncated pyramid-like structure, as shown in Fig. 6. Such a structure provides good solid angle coverage while keeping incident angles close to 90 degrees, thus reducing the dead layer effect on the detector's energy resolution. Two pyramid structures will be positioned equidistantly from the catcher

plane in the final setup. Although the detection system is located in the cold bore of the superconducting magnet, an additional active cooling system will be used to speed up the thermalization process. Custom made low-noise preamplifier cards based on the CAEN preamplifiers A1422H [31] were designed to achieve high energy resolution. The resolution FWHM of the front strip preamplifiers, determined using a pulser and a 100 pF capacitance load, was found to be below 4.5 keV for each channel.

According to the specification data, the detectors have a state-of-the-art dead-layer thickness not exceeding 100 nm. However, to make sure that the performance of the detectors meets the stringent requirements of the WISArD experiment, a prototype detector was supplied by Micron to be studied at LP2i Bordeaux. Test measurements at the AIFIRA accelerator [32] using a 700 keV alpha beam were performed. On average, the detector resolution was determined to be 9 ± 3 keV (FWHM) for all five strips. Additionally, the detector was rotated by 45 degrees to measure the dead layer thickness. The dead layer was studied at two positions (center and edge) and was found to be 60.5 ± 3.6 nm. Additional measurements mapping the dead layer thickness over the entire detector surface for all detectors showed that the variation is of the order of 100 nm, i.e. within the manufacturing specification.

A Monte-Carlo simulation using Geant4 [33–35] was used to estimate the solid angle coverage for 3.3 MeV protons emitted from the catcher plane of the detection system in a 4 T magnetic field. The solid angle was determined by comparing the total number of emitted protons versus those registered in the active area of the detectors, the latter being placed at various distances. The maximum coverage achieved was 57% for a distance of 20 mm between the two pyramids. A major constraint in the final separation is the space required for the rotatable mounts of the beam diagnostics, the calibration source and the catcher foil.

3.4. Plastic scintillator and front-end electronics

The second significant improvement in the WISArD detection setup concerns the beta detector. The detection principle remains based on a plastic scintillator coupled to silicon photomultipliers (SiPMs), but modifications were made to lower the detection threshold as much as possible. A low detection threshold is crucial to limit the effect of backscattering. Beta particles impinging on the plastic scintillator have a certain probability of backscattering, increasing with more grazing angles, leaving only a fraction of their energy in the detector. Therefore, a lower detection threshold reduces the need for simulations to evaluate the missing events below the threshold. In the upgrade, the diameter of the plastic scintillator is increased from 20 to 30 mm. Its length remains 50 mm, sufficient to stop positrons up to 10 MeV. An EJ200 *polyvinyltoluene* scintillator from ELJEN [36] is used.
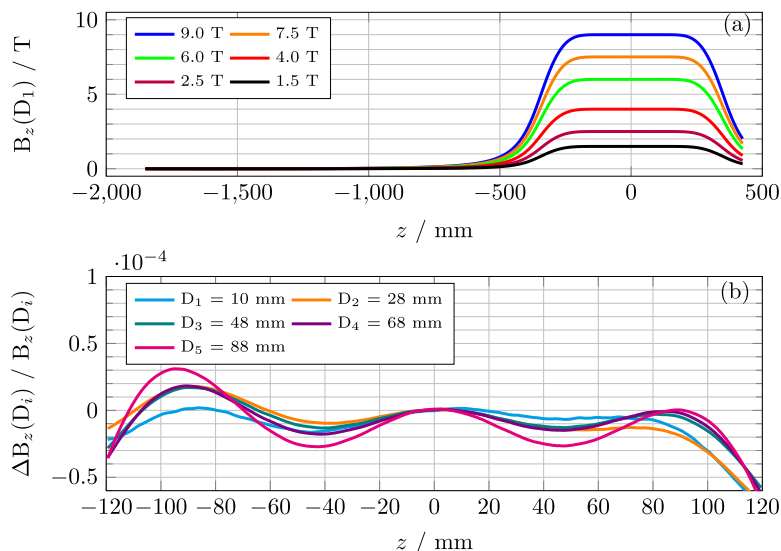
Fig. 5. Panel (a): Measurements of the absolute axial magnetic profile for various field levels. Panel (b): The relative axial profile given at 4 T (used in Nov2018 run) as measured at different surfaces by five concentric disks (D1: smallest; D5: biggest). Profiles are normalized to the central field.
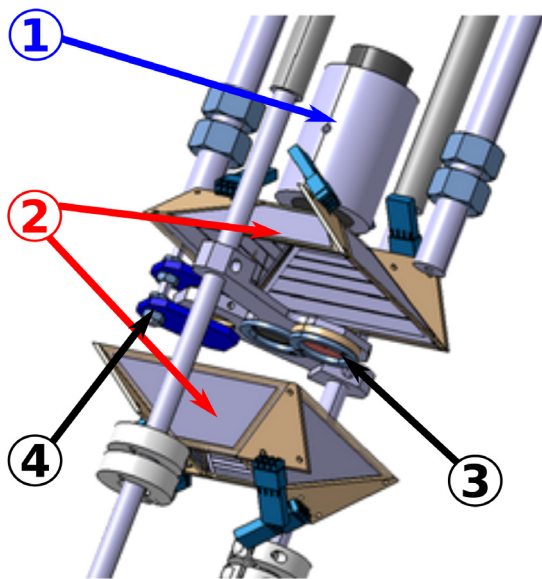

Fig. 6. The new design of the detector assembly of WISArD. (1) Housing of the plastic scintillator coupled to the SiPM array for detecting beta particles. (2) Two pyramid-like hemispheres of eight silicon detectors to detect the beta-delayed protons. (3) Arm to hold the Mylar foil used for implantation of the ISOLDE RIB and a beam diagnostics, i.e. MCP or Faraday Cup. (4) Arm holding the calibration alpha source placed in the parking position.

Fig. 7. CAD drawing of the SiPM array seen through the plastic scintillator. Nine individual SiPMs are visible on the back side of the scintillator. Furthermore, one can see the front-end electronics composing the high and low gain amplification stages (see text for details).

The light output is collected at the back of the scintillator by an array of 3×3 MicroFJ-60035-TSV-TR1, J-Series type 6×6 mm^2 SiPM sensors, from ONSEMI (formerly SensL) [37]. Each sensor is wired to a preamplifier, designed and tailor-made by IFIN-HH in Bucharest [38]. All preamplifiers are equipped with a minimal pulse shaping network to provide an increased signal to noise ratio and, at the same time, reduce the pulse width of the output signals. Fig. 7 shows the SiPM array connected to the scintillator with optical grease. In this configuration, the geometrical efficiency for light collection increases by about one order of magnitude compared to the configuration of the DSet2018 experiment. Each SiPM preamplifier features a dual-range output. The low-gain (LG) output allows us to measure the full beta spectrum, while the high-gain (HG) output is used to precisely characterize the detection threshold. With the SiPMs biased at their nominal operating voltage
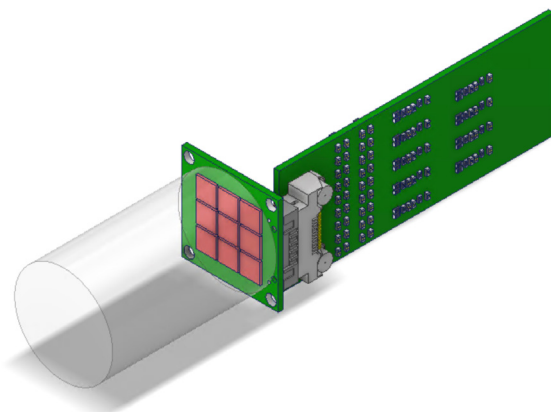
(27 V), a factor of ten in signal amplitude between HG (600 ± 10 mV) and LG (60 ± 10 mV) was verified with monoenergetic α particles from ^{241}Am. The difference in amplification was also measured with monoenergetic electrons at LP2i Bordeaux. An example spectrum for electron energy of 1 MeV delivered by an electron spectrometer [39] is shown in Fig. 8 (a). Furthermore, the calibration of the LG outputs of the detector used monoenergetic electrons in the 0.7–1.8 MeV energy range. The energy resolution of the spectrometer is of the order of 1%. Fig. 8 (b) shows that the typical response function of the SiPMs is not completely a Gaussian. The behavior of the detector coupled to the SiPM array assembly was verified to be linear at different bias voltages around the nominal operating voltage of 27 V. Typical calibration plots for a single sensor of the SiPM array are shown in Fig. 9. Each point was obtained by fitting a normal distribution to a restricted region of the raw spectrum obtained after collecting data from a fixed energy of the electron spectrometer. During the selection one avoided as much as possible the low-energy tail coming from electron backscattering etc. The mean of the normal distribution is given in QDC channel number (see Section 3.5 on the QDC channel description). The expected increase in gain due to the decreasing temperature inside the bore can thus be adjusted by modifying the operating voltage. A typical
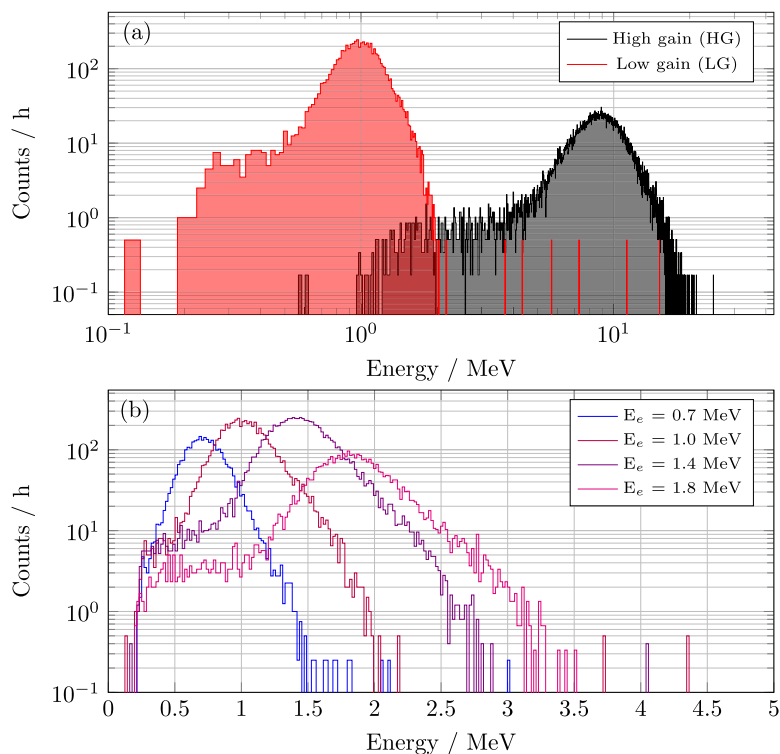
Fig. 8. Panel (a): Difference in the high and low gain amplification for one SiPM. The spectrometer was set to an electron energy of 1 MeV. Panel (b): Comparison of the LG response function for different electron energies.
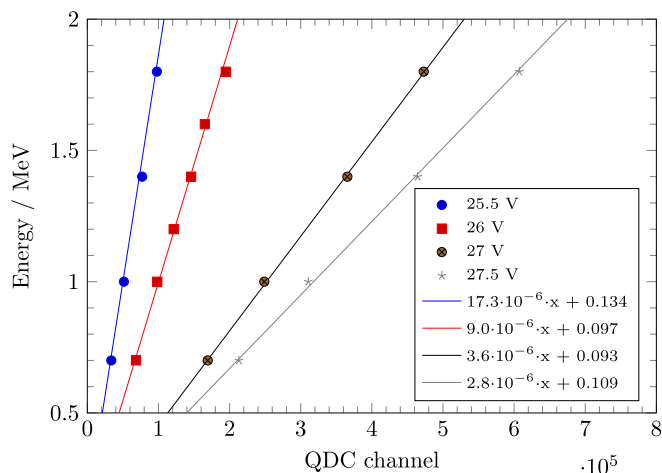

Fig. 9. Study of the energy dependence as a function of the bias voltage for one of the sensors from the SiPM array. Uncertainties are smaller than the point size. Each point was obtained after fitting a Normal distribution to a restricted range around the maximum of the peaks. This was done to avoid contribution from electron backscattering that is visible in the low energies (see Fig. 8). Lines are fits to the data points with the respective coefficients given in the legend.

resolution of the beta particle detector was found to be of about 13% FWHM at 1 MeV.

3.5. Data acquisition

The signal pulses produced by all detectors are processed by the FASTER data acquisition system, developed by LPC CAEN [40]. FASTER is a high-performance, modular digital acquisition system based on a synchronized tree model. In particular, forty-eighth ADC channels (MOSHAR) are employed to digitize the proton signals from the silicon detectors. The MOSHAR module was developed for spectroscopy measurement and provides a 14 bits with up-to 125 MHz ADC capability. Another eighteen QDC channels (CARAS) are used to process the β-particle signals sent by both LG and HG outputs from each individual SiPM sensor. The CARAS module features a 12 bits ADC capability with 500 MHz.

The DAQ configuration allows to be running in the so-called *lossless mode*, so that all processed events are preserved on disk. Furthermore, a *trigger-merger* configuration defines how events in the data tree are flagged. In our case we require at least three HG SiPM sensors to be triggered within a 200 ns time window to be considered as a beta event. If any of the silicon detector pulses occur in a time window with up to 1 µs before and 2 µs after the beta event, it will be flagged as *coincidence* event. This allows online monitoring of the β-gated kinematic shift in the proton energy spectra.

For ADC channels, the data sent to the PC comprises the timestamp of the first triggering cell, the maximum height of the signal (in mV) after proper filtering by a CRRC4 filter, a time reference for this maximum (relative to the trigger), a pile-up flag indicating an eventual pile-up event, and a saturation flag saying when the signal height was higher than the maximum voltage range. In case of QDC channels, the charge of the digitized signals can be integrated over up to four different time windows. The data sent to the PC comprises the time stamp of the trigger, the integrated charges and a saturation flag.

3.6. Beam implantation monitoring

The study of systematic effects subsequent to the DSet2018 experiment has shown that, in order to reach the per mil precision level on $\tilde{a}$, the implantation profile in the catcher foil has to be determined with a spatial precision better than 0.5 mm [17]. For this purpose, a compact microchannel plate (MCP) position sensitive detector has been designed (Fig. 10 (a)). It is a 10 mm thick and 25 mm in diameter detector with an active detection diameter of 15 mm. The detector assembly is mounted on a rotatable rod opposite to the one holding
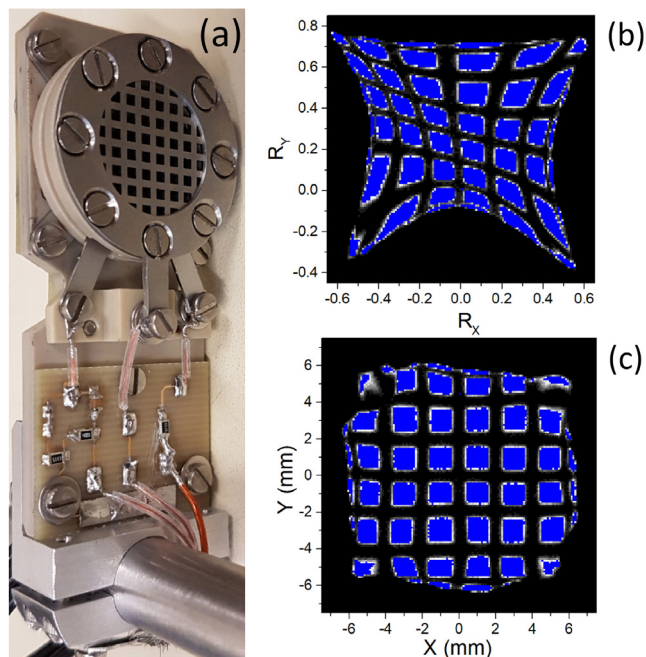
Fig. 10. Picture of the MCP detector assembly (a), mask image reconstruction using charge sharing ratios (b) and mask image reconstruction after additional numerical treatment (c).

the catcher and can be inserted in front of the latter to measure the profile of the incoming beam. The ion detection and impact position measurement are based on the use of three MCPs mounted in a Z-stack configuration, followed by a square resistive anode made of graphite paint. After the impact of an incoming ion, the electron avalanche emitted by the back MCP is collected by the resistive anode which provides information on the impact position through the measurement of the charge sharing between its four corners. A 0.5 mm thick stainless steal calibration mask composed of 1.2×1.2 mm^2 square holes with a pitch of 2 mm is permanently mounted in front of the MCPs to provide an accurate position calibration. Fig. 10 (b) shows the distribution of the charge ratios R_X and R_Y obtained when irradiating the detector with alpha particles emitted by a ^{241}Am source located 80 mm away from the mask. The R_X (R_Y) coordinates are here directly inferred from the difference between the charges collected on the right (up) corners and the left (down) corners, divided by the sum of charges. The distortions due to the square shape of the anode and to inhomogeneities in the graphite paint thickness require the use of an additional numerical treatment. Polynomial functions depending on R_X and R_Y are thus used to reconstruct a realistic position in X and Y matching the mask dimensions. Fig. 10 (c) shows an example of such a reconstruction obtained with polynomial functions of order 5 resulting from a multi-dimensional fit of the mask image. A detailed analysis of this image has demonstrated that for the central part of the detector (within a 8 mm diameter circle), the spatial resolution (FWHM) in X and Y is better than 0.25 mm and the accuracy better than 0.1 mm. The present results fulfill the needs for beam monitoring, but additional tests will still have to be performed. In particular, it is known that a strong magnetic field decreases the gain of the MCPs. These calibrations will thus have to be completed in situ, within the WISArD detection chamber and with magnetic fields up to 4 T. A thin 10% transmission mesh will also be inserted right behind the calibration mask in order to both attenuate the ion beam intensity prior to hitting the front MCP and serve as a Faraday cup for beam current measurement.

3.7. Monte Carlo simulations benchmark

A Monte Carlo simulation of particle transport in the detection setup is essential for the analysis of the data and the extraction of $\tilde{a}$. The geometry of the setup in the simulations must be validated against calibration data. For this purpose, tests with different radioactive alpha and beta sources were performed in July 2019. Seven of the runs used a multiple α-source, made of ^{148}Gd, ^{239}Pu, ^{241}Am and ^{244}Cm (A_{total} = 4.6 kBq) and thirteen runs with a ^{207}Bi source (A = 20.9 kBq). The results were then compared with simulations based on Geant4 v10.5.p01.

3.7.1. Particle transport and detector geometry

In the case of the alpha source, simulations were used to validate the particle transport within the magnetic field and the detectors geometry as implemented in our simulations. Differences between experimental and simulated detection efficiency for all detectors as a function of the magnetic field are shown in Fig. 11. Note that during the measurements, detector Si4D was disconnected. The experimental detection efficiencies are determined as the integral recorded by each silicon detector at the alpha energy. Then, all efficiencies are normalized to the corresponding value at $B = 0$ T for easy comparison. Systematic errors have been evaluated by adjusting detectors' positions with respect to the simulated design. The values are in all cases compatible with zero, i.e. within 1σ (79.3% of measurements) and 2σ (20.7% of measurements). The maximal discrepancy corresponds to a value of $9.4\% \pm 4.9\%_{stat} \pm 4.7\%_{syst}$.

3.7.2. Positron backscattering

The effect of positron backscattering takes place inside the catcher foil and on the surface of the plastic scintillator. In the latter case, the backscattered positrons cannot deposit their full initial energy in the plastic scintillator, potentially leading to missing or misidentified beta-delayed proton events in the data analysis. Precise characterization of the backscattering in our case is possible via Monte Carlo simulations.

In the decay of ^{207}Bi both γ-rays and electrons contribute to the observed spectrum. Increasing the magnetic field strength increases the collection efficiency for electrons, but not for the gamma rays. Subtracting the spectrum obtained at $B = 0$ T during the same acquisition time removes the gamma contribution, leaving a clean electron spectrum to be compared with simulations.

In the simulations we used different Geant4 physics lists (*Penelope, Livermore, LowEMEnergyPhysics, EMstandard opt4, Goudsmit–Saunderson*). The energy-calibrated QDC spectra and the simulated spectra convoluted with the detector's response function have been superimposed and quantitatively compared. A complete exploration of the parameter space has been done to determine the calibration and response function parameters that minimize the χ^2 value between experimental and simulated histograms. The energy calibration used in the minimization procedure was of the form $E = a + b \cdot C + c \cdot C^2$, while the detector resolution was extracted as $\sigma = d + e \cdot \sqrt{E}$, where C is the QDC channel number and a, b, c, d, e are the calibration and detector's response function parameters. An example comparing experimental and simulated runs is shown in Fig. 12. The typical electron conversion spectrum of ^{207}Bi exposes several features of the beta detector, i.e. the four conversion electron peaks at 482, 555, 976 and 1049 keV are not separated. Instead, the detector's resolution is sufficient only to resolve the two groups at around 500 keV and 1000 keV. The peak at 1.5 MeV corresponds to adding the individual conversion electron groups within the detection window. At the present level of detector resolution, all Geant4 models show similar behavior.

Further tests aiming to precisely constrain and characterize the Geant4 simulations in the low-energy region of the β spectra, in which the backscattering continuum is principally located, are ongoing with different and independent experimental setups. The aim of these measurements is to put an uncertainty limit on the Geant4 simulations for future WISArD experiments.
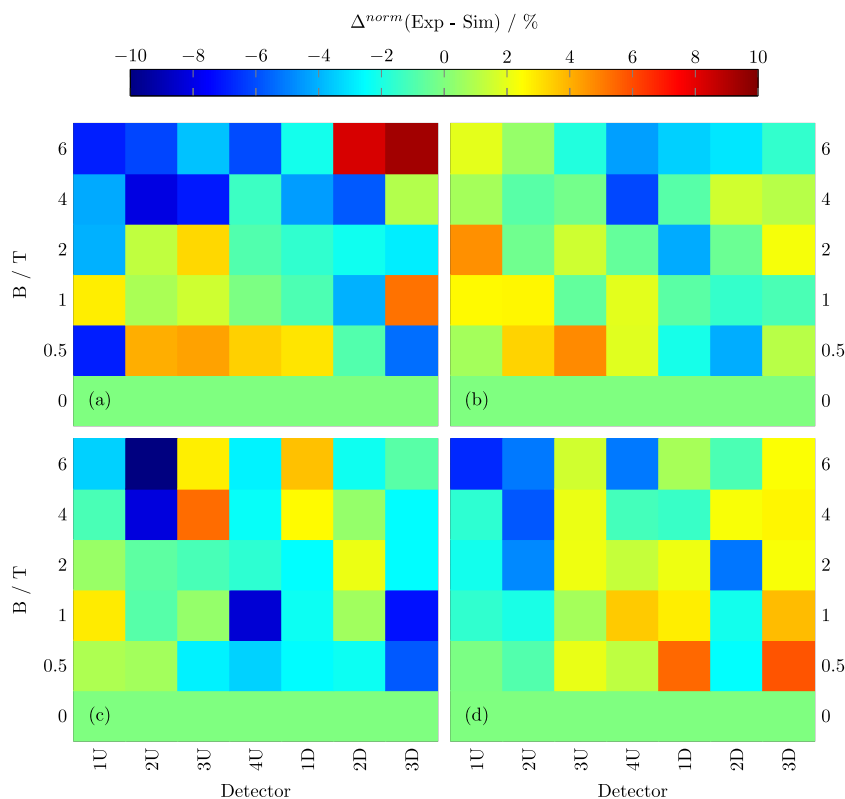
$$\Delta^{norm}(\text{Exp - Sim}) \ / \ \%$$

Fig. 11. Differences between normalized experimental and simulated detection efficiencies for all active silicon detectors as a function of the magnetic field strength. The Δ was normalized to acquisition time and magnetic field strength, where subplot (a) is given for ^{148}Gd ($E_\alpha = 3182.690$ keV), (b) for ^{239}Pu ($E_\alpha = 5244.50$ keV), (c) for ^{241}Am ($E_\alpha = 5637.82$ keV) and (d) for ^{244}Cm ($E_\alpha = 5901.74$ keV). See text for more details on the normalization procedure.
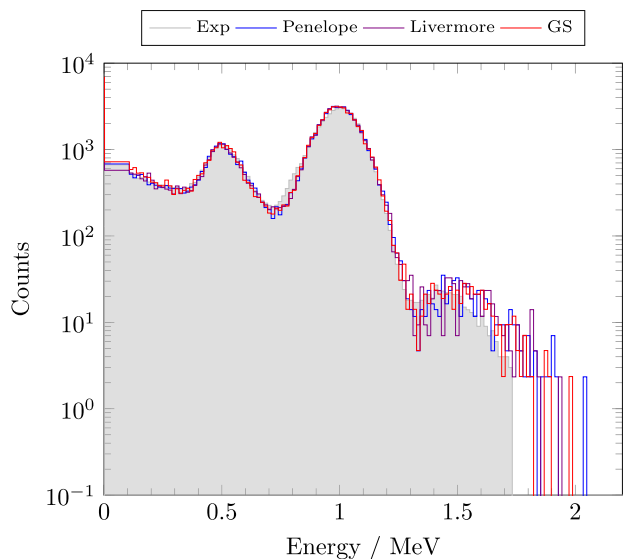

Fig. 12. Comparison between experimental and simulated Geant4 spectra for ^{207}Bi measured at $B = 4$ T. The calibrated experimental spectrum from this run is given in gray color (an energy cut was applied at 1.66 MeV). The Geant4 simulations using the following physics lists : *Penelope* (blue), *Livermore* (violet), and *Goudsmit-Saunderson* (GS, red) have been used. The calibration parameters for this specific run are $a = 2000$ keV, $b = 97519$ keV/C, $c = 9500$ keV/C^2, $d = 761$ keV and $e = 8891$ $\sqrt{keV}$ with χ^2/N_{dof} being 3.82 (*Penelope*), 4.29 (*Livermore*), and 3.69 (*GS*). For explanation of the different parameters, see Section 3.7.2.

Table 2
A summary of the achieved performance in the test run in 2022 for the IAS of ^{32}Ar.

	Source	Uncertainty [Nov2018]	Uncertainty [Oct2022]
Det. System	Detector position	1 mm	0.1 mm
	Source position	3 mm	0.1 mm
	Source radius	3 mm	0.1 mm
	Magnetic field	1%	0.001%
Protons	Average Abs. Resolution	40 keV	15 keV
	Average Dead Layer	300 nm	20 nm
Positrons	Detection threshold	12 keV	10 keV

in the WISArD setup. After the Proof-of-Principle experiment we have identified potential improvements in the setup to reduce systematic effects and improve gathering statistics. A major part includes the tailor-made detection setup and the ion-beam handling. A new test run was performed at ISOLDE in October 2021, showing promising improvements with respect to DSet2018 [41]. For the statistical uncertainty, an overall reduction by a factor of two was achieved. This improvement is even more significant given that it was obtained with only half of the previously required beam time. The gain factor expected from the upgrades is now evaluated to be in the range of 40. A summary of the achieved uncertainties so far studied is given in Table 2. A full scale experiment is foreseen for middle of 2023.

CRediT authorship contribution statement

D. Atanasov: Writing – original draft, Formal analysis, Visualization. **F. Cresto:** Writing – original draft, Formal analysis. **L. Nies:** Writing – original draft, Formal analysis. **M. Pomorski:** Writing – original draft, Formal analysis. **M. Versteegen:** Writing – original draft, Formal analysis. **P. Alfaurt:** Methodology, Investigation, Writing – review & editing. **V. Araujo-Escalona:** Investigation, Writing – review

4. Summary

In summary, we have described the beamline for beta-neutrino angular correlations measurements by using beta-delayed proton emission

& editing. **P. Ascher:** Investigation, Writing – review & editing. **B. Blank:** Conceptualization, Investigation, Writing – review & editing. **L. Daudin:** Software, Investigation, Writing – review & editing. **D. Guillet:** Investigation, Writing – review & editing. **X. Fléchard:** Conceptualization, Writing – review & editing. **J. Ha:** Investigation, Writing – review & editing. **A. Husson:** Investigation, Writing – review & editing. **M. Gerbaux:** Investigation, Writing – review & editing. **J. Giovinazzo:** Software, Investigation, Writing – review & editing. **S. Grévy:** Investigation, Writing – review & editing. **T. Kurtukian-Nieto:** Investigation, Writing – review & editing. **L. Leterrier:** Methodology, Investigation, Writing – review & editing. **R. Lica:** SiPM array and readout, Funding acquisition. **E. Liénard:** Investigation, Writing – review & editing. **C. Mihai:** SiPM array and readout, Funding acquisition. **C. Neacsu:** SiPM array and readout, Conceptualization, Review, Validation, Project administration. **A. Ortega-Moral:** Investigation, Writing – review & editing. **G. Pascovici:** SiPM array and readout, Conceptualization, Review. **M. Roche:** Methodology, Investigation, Writing – review & editing. **N. Severijns:** Conceptualization, Writing – review & editing. **S. Vanlangendonck:** Investigation, Writing – review & editing. **A. Welker:** Investigation. **D. Zákoucký:** Investigation, Writing – review & editing.

Declaration of competing interest

The authors declare that they have no known competing financial interests or personal relationships that could have appeared to influence the work reported in this paper.

Data availability

Data will be made available on request.

References

[1] J. Beringer, et al., Particle Data Group Collaboration, Review of particle physics, Phys. Rev. D 86 (2012) 010001, http://dx.doi.org/10.1103/PhysRevD.86.010001.

[2] M. González-Alonso, O. Naviliat-Cuncic, N. Severijns, New physics searches in nuclear and neutron β decay, Prog. Part. Nucl. Phys. 104 (2019) 165–223, http://dx.doi.org/10.1016/j.ppnp.2018.08.002.

[3] L. Hayen, N. Severijns, K. Bodek, D. Rozpedzik, X. Mougeot, High precision analytical description of the allowed β spectrum shape, Rev. Modern Phys. 90 (2018) 015008, http://dx.doi.org/10.1103/RevModPhys.90.015008.

[4] J.D. Jackson, S.B. Treiman, H.W. Wyld, Possible tests of time reversal invariance in beta decay, Phys. Rev. 106 (1957) 517–521, http://dx.doi.org/10.1103/PhysRev.106.517.

[5] M. González-Alonso, O. Naviliat-Cuncic, Kinematic sensitivity to the fierz term of β-decay differential spectra, Phys. Rev. C 94 (2016) 035503, http://dx.doi.org/10.1103/PhysRevC.94.035503.

[6] A. Falkowski, M. González-Alonso, O. Naviliat-Cuncic, Comprehensive analysis of beta decays within and beyond the standard model, J. High Energy Phys. 4 (2021) 1–36, http://dx.doi.org/10.1007/JHEP04(2021)126.

[7] A. Gorelov, D. Melconian, W.P. Alford, D. Ashery, G. Ball, J.A. Behr, P.G. Bricault, J.M. D'Auria, J. Deutsch, J. Dilling, M. Dombsky, P. Dubé, J. Fingler, U. Giesen, F. Glück, S. Gu, O. Häusser, K.P. Jackson, B.K. Jennings, M.R. Pearson, T.J. Stocki, T.B. Swanson, M. Trinczek, Scalar interaction limits from the $\beta - \nu$ correlation of trapped radioactive atoms, Phys. Rev. Lett. 94 (2005) 142501, http://dx.doi.org/10.1103/PhysRevLett.94.142501.

[8] P.A. Vetter, J.R. Abo-Shaeer, S.J. Freedman, R. Maruyama, Measurement of the $\beta - \nu$ correlation of ^{21}Na using shakeoff electrons, Phys. Rev. C 77 (2008) 035502, http://dx.doi.org/10.1103/PhysRevC.77.035502.

[9] M.G. Sternberg, R. Segel, N.D. Scielzo, G. Savard, J.A. Clark, P.F. Bertone, F. Buchinger, M. Burkey, S. Caldwell, A. Chaudhuri, J.E. Crawford, C.M. Deibel, J. Greene, S. Gulick, D. Lascar, A.F. Levand, G. Li, A. Pérez Galván, K.S. Sharma, J. Van Schelt, R.M. Yee, B.J. Zabransky, Limit on tensor currents from ^{8}Li β decay, Phys. Rev. Lett. 115 (2015) 182501, http://dx.doi.org/10.1103/PhysRevLett.115.182501.

[10] M. Beck, F. Ayala Guardia, M. Borg, J. Kahlenberg, R. Muñoz Horta, C. Schmidt, A. Wunderle, W. Heil, R. Maisonobe, M. Simson, T. Soldner, R. Virot, O. Zimmer, M. Klopf, G. Konrad, S. Baeßler, F. Glück, U. Schmidt, Improved determination of the $\beta - \bar{\nu}_e$ angular correlation coefficient a in free neutron decay with the aSPECT spectrometer, Phys. Rev. C 101 (2020) 055506, http://dx.doi.org/10.1103/PhysRevC.101.055506.

[11] X. Fléchard, P. Velten, E. Liénard, A. Méry, D. Rodríguez, G. Ban, D. Durand, F. Mauger, O. Naviliat-Cuncic, J.C. Thomas, Measurement of the $\beta-\nu$ correlation coefficient a$\beta\nu$ in the β decay of trapped 6he+ ions, J. Phys. G: Nucl. Part. Phys. 38 (5) (2011) 055101, http://dx.doi.org/10.1088/0954-3899/38/5/055101.

[12] P.D. Shidling, V.S. Kolhinen, B. Schroeder, N. Morgan, A. Ozmetin, D. Melconian, TAMUTRAP facility: Penning trap facility for weak interaction studies, Hyperfine Interact. 240 (1) (2019) 055101, http://dx.doi.org/10.1007/s10751-019-1584-9.

[13] E.G. Adelberger, C. Ortiz, A. García, H.E. Swanson, M. Beck, O. Tengblad, M.J.G. Borge, I. Martel, H. Bichsel, the ISOLDE Collaboration, Positron-neutrino correlation in the $0^{+}\rightarrow 0^{+}$ decay of ^{32}Ar, Phys. Rev. Lett. 83 (1999) 1299–1302, http://dx.doi.org/10.1103/PhysRevLett.83.1299.

[14] E. Clifford, E. Hagberg, J. Hardy, H. Schmeing, R. Azuma, H. Evans, V. Koslowsky, U. Schrewe, K. Sharma, I. Towner, The decay of 20Na: Measurements of isospin mixing and the weak vector coupling constant as well as other new decay data, Nuclear Phys. A 493 (2) (1989) 293–322, http://dx.doi.org/10.1016/0375-9474(89)90399-0, URL http://www.sciencedirect.com/science/article/pii/0375947489903990.

[15] V. Vorobel, C. Briançon, V. Brudanin, V. Egorov, J. Deutsch, R. Prieels, N. Severijns, Y. Shitov, C. Vieu, T. Vylov, I. Yutlandov, S. Zaparov, Beta-neutrino angular correlation in the decay of ^{14}o - scalar coupling and interatomic interaction, Eur. Phys. J. A 16 (1) (2003) 139–147, http://dx.doi.org/10.1140/epja/i2002-10067-y.

[16] V. Egorov, C. Briançon, V. Brudanin, J. Dionisio, J. Deutsch, V. Gorozhankin, Y. Gurov, R. Prieels, V. Sandukovsky, N. Severijns, M. Simoes, Y. Shitov, C. Vieu, V. Vorobel, T. Vylov, I. Yutlandov, S. Zaparov, Beta-neutrino angular correlation in the decay of 18Ne, Nuclear Phys. A 621 (3) (1997) 745–753, http://dx.doi.org/10.1016/S0375-9474(97)00178-4, URL https://www.sciencedirect.com/science/article/pii/S0375947497001784.

[17] V. Araujo-Escalona, D. Atanasov, X. Fléchard, P. Alfaurt, P. Ascher, B. Blank, L. Daudin, M. Gerbaux, J. Giovinazzo, S. Grévy, T. Kurtukian-Nieto, E. Liénard, G. Quéméner, N. Severijns, S. Vanlangendonck, M. Versteegen, D. Zákoucký, Simultaneous measurements of the β-neutrino angular correlation in ^{32}Ar pure Fermi and pure Gamow-Teller transitions using β-proton coincidences, Phys. Rev. C 101 (2020) 055501, http://dx.doi.org/10.1103/PhysRevC.101.055501.

[18] V. Cirigliano, A. Garcia, D. Gazit, O. Naviliat-Cuncic, G. Savard, A. Young, Precision beta decay as a probe of new physics, 2019, http://dx.doi.org/10.48550/arxiv.1907.02164, arXiv URL https://arxiv.org/abs/1907.02164v2.

[19] E. Kugler, The ISOLDE facility, Hyperfine Interact. 129 (1) (2000) 23–42, http://dx.doi.org/10.1023/A:1012603025802.

[20] M.J.G. Borge, K. Blaum, Focus on exotic beams at ISOLDE: A laboratory portrait, J. Phys. G: Nucl. Part. Phys. 45 (1) (2017) 010301, http://dx.doi.org/10.1088/1361-6471/aa990f.

[21] J.P. Ramos, A. Gottberg, R.S. Augusto, T.M. Mendonca, K. Riisager, C. Seiffert, P. Bowen, A.M. Senos, T. Stora, Target nanomaterials at CERN-ISOLDE: synthesis and release data, Nucl. Instrum. Methods Phys. Res. B 376 (2016) 81–85, http://dx.doi.org/10.1016/J.NIMB.2016.03.003.

[22] L. Penescu, R. Catherall, J. Lettry, T. Stora, Development of high efficiency versatile arc discharge ion source at CERN ISOLDE, Rev. Sci. Instrum. 81 (2) (2010) 02A906, http://dx.doi.org/10.1063/1.3271245.

[23] V. Kozlov, N. Severijns, D. Beck, M. Beck, S. Coeck, B. Delauré, A. Lindroth, S. Kopecky, P. Delahaye, F. Wenander, V. Golovko, I. Kraev, T. Phalet, The WITCH experiment: Completion of a set-up to investigate the structure of weak interactions with a penning trap, Int. J. Mass Spectrom. 251 (2) (2006) 159–172, http://dx.doi.org/10.1016/j.ijms.2006.01.050, ULTRA-ACCURATE MASS SPECTROMETRY AND RELATED TOPICS Dedicated to H.-J. Kluge on the occasion of his 65th birthday anniversary, URL http://www.sciencedirect.com/science/article/pii/S1387380606000789.

[24] O. Forstner, Beam-preparation with REXTRAP for the REX-ISOLDE experiment (Ph.D. thesis), Technische Universität Wien, 2001.

[25] S. Project, F. Piquemal, Proceedings of the 5th international conference on nonaccelerator new PHYSICS double-beta decay and rare processes, Phys. Atomic Nucl. 69 (2006) 2096–2100, http://dx.doi.org/10.1134/S1063778806120131.

[26] R. Hodák, M. Bukový, H. Burešová, C. Cerna, L. Fajt, J. Jouve, P. Kouba, C. Marquet, F. Piquemal, P. Přidal, K. Smolek, M. Špavorová, I. Štekl, Improvement of the energy resolution of the scintillating detectors for the low background measurement, AIP Conf. Proc. 1672 (2015) http://dx.doi.org/10.1063/1.4928013.

[27] D. Manura, D. Dahl, SIMION (R) 8.1 User Manual (Adaptas Solutions, LLC, Palmer, MA 01069), 2008, http://simion.com/.

[28] L. Nies, D. Atanasov, V. Auraujo-Escalona, Progress towards WISArD: Beam line simulations and detector studies for the Weak Interaction Studies with 32Ar Decay (WISArD) experiment, Summer Student 2018 Report, 2018, URL https://cds.cern.ch/record/2639863.

[29] C. Petrone, B. Bordini, M. Buzio, S. Russenschuck, A transducer for measuring the field quality in superconducting solenoids, IEEE Trans. Appl. Supercond. 30 (4) (2020) 1–5, http://dx.doi.org/10.1109/TASC.2020.2971446.

[30] Micron semiconductor ltd, 2022, http://www.micronsemiconductor.co.uk/.

[31] Caen spa, 2022, https://www.caen.it/products/a1422h/.

[32] P. Barberet, J. Jouve, S. Sorieul, P. Alfaurt, L. Mathieu, AIFIRA: a light ion beam facility for ion beam analysis and irradiation, Eur. Phys. J. Plus 136 (2021) 1–10, http://dx.doi.org/10.1140/EPJP/S13360-020-01045-9, URL https://link.springer.com/article/10.1140/epjp/s13360-020-01045-9.

[33] S. Agostinelli, J. Allison, K. Amako, J. Apostolakis, H. Araujo, P. Arce, M. Asai, D. Axen, S. Banerjee, G. Barrand, F. Behner, L. Bellagamba, J. Boudreau, L. Broglia, A. Brunengo, H. Burkhardt, S. Chauvie, J. Chuma, R. Chytracek, G. Cooperman, G. Cosmo, P. Degtyarenko, A. Dell'Acqua, G. Depaola, D. Dietrich, R. Enami, A. Feliciello, C. Ferguson, H. Fesefeldt, G. Folger, F. Foppiano, A. Forti, S. Garelli, S. Giani, R. Giannitrapani, D. Gibin, J.J.G. Cadenas, I. Gonzalez, G.G. Abril, G. Greeniaus, W. Greiner, V. Grichine, A. Grossheim, S. Guatelli, P. Gumplinger, R. Hamatsu, K. Hashimoto, H. Hasui, A. Heikkinen, A. Howard, V. Ivanchenko, A. Johnson, F.W. Jones, J. Kallenbach, N. Kanaya, M. Kawabata, Y. Kawabata, M. Kawaguti, S. Kelner, P. Kent, A. Kimura, T. Kodama, R. Kokoulin, M. Kossov, H. Kurashige, E. Lamanna, T. Lampen, V. Lara, V. Lefebure, F. Lei, M. Liendl, W. Lockman, F. Longo, S. Magni, M. Maire, E. Medernach, K. Minamimoto, P.M. de Freitas, Y. Morita, K. Murakami, M. Nagamatu, R. Nartallo, P. Nieminen, T. Nishimura, K. Ohtsubo, M. Okamura, S. O'Neale, Y. Oohata, K. Paech, J. Perl, A. Pfeiffer, M.G. Pia, F. Ranjard, A. Rybin, S. Sadilov, E. di Salvo, G. Santin, T. Sasaki, N. Savvas, Y. Sawada, S. Scherer, S. Sei, V. Sirotenko, D. Smith, N. Starkov, H. Stoecker, J. Sulkimo, M. Takahata, S. Tanaka, E. Tcherniaev, E.S. Tehrani, M. Tropeano, P. Truscott, H. Uno, L. Urban, P. Urban, M. Verderi, A. Walkden, W. Wander, H. Weber, J.P. Wellisch, T. Wenaus, D.C. Williams, D. Wright, T. Yamada, H. Yoshida, D. Zschiesche, Geant4—a simulation toolkit, Nucl. Instrum. Methods Phys. Res. A 506 (2003) 250–303, http://dx.doi.org/10.1016/S0168-9002(03)01368-8.

[34] J. Allison, K. Amako, J. Apostolakis, H. Araujo, P. Arce Dubois, M. Asai, G. Barrand, R. Capra, S. Chauvie, R. Chytracek, G. Cirrone, G. Cooperman, G. Cosmo, G. Cuttone, G. Daquino, M. Donszelmann, M. Dressel, G. Folger, F. Foppiano, J. Generowicz, V. Grichine, S. Guatelli, P. Gumplinger, A. Heikkinen, I. Hrivnacova, A. Howard, S. Incerti, V. Ivanchenko, T. Johnson, F. Jones, T. Koi, R. Kokoulin, M. Kossov, H. Kurashige, V. Lara, S. Larsson, F. Lei, O. Link, F. Longo, M. Maire, A. Mantero, B. Mascialino, I. McLaren, P. Mendez Lorenzo, K. Minamimoto, K. Murakami, P. Nieminen, L. Pandola, S. Parlati, L. Peralta, J. Perl, A. Pfeiffer, M. Pia, A. Ribon, P. Rodrigues, G. Russo, S. Sadilov, G. Santin, T. Sasaki, D. Smith, N. Starkov, S. Tanaka, E. Tcherniaev, B. Tome, A. Trindade, P. Truscott, L. Urban, M. Verderi, A. Walkden, J. Wellisch, D. Williams, D. Wright, H. Yoshida, Geant4 developments and applications, IEEE Trans. Nucl. Sci. 53 (1) (2006) 270–278, http://dx.doi.org/10.1109/TNS.2006.869826.

[35] J. Allison, K. Amako, J. Apostolakis, P. Arce, M. Asai, T. Aso, E. Bagli, A. Bagulya, S. Banerjee, G. Barrand, B.R. Beck, A.G. Bogdanov, D. Brandt, J.M. Brown, H. Burkhardt, P. Canal, D. Cano-Ott, S. Chauvie, K. Cho, G.A. Cirrone, G. Cooperman, M.A. Cortés-Giraldo, G. Cosmo, G. Cuttone, G. Depaola, L. Desorgher, X. Dong, A. Dotti, V.D. Elvira, G. Folger, Z. Francis, A. Galoyan, L. Garnier, M. Gayer, K.L. Genser, V.M. Grichine, S. Guatelli, P. Guèye, P. Gumplinger, A.S. Howard, I. Hřivnáčová, S. Hwang, S. Incerti, A. Ivanchenko, V.N. Ivanchenko, F.W. Jones, S.Y. Jun, P. Kaitaniemi, N. Karakatsanis, M. Karamitrosi, M. Kelsey, A. Kimura, T. Koi, H. Kurashige, A. Lechner, S.B. Lee, F. Longo, M. Maire, D. Mancusi, A. Mantero, E. Mendoza, B. Morgan, K. Murakami, T. Nikitina, L. Pandola, P. Paprocki, J. Perl, I. Petrović, M.G. Pia, W. Pokorski, J.M. Quesada, M. Raine, M.A. Reis, A. Ribon, A.R. Fira, F. Romano, G. Russo, G. Santin, T. Sasaki, D. Sawkey, J.I. Shin, I.I. Strakovsky, A. Taborda, S. Tanaka, B. Tomé, T. Toshito, H.N. Tran, P.R. Truscott, L. Urban, V. Uzhinsky, J.M. Verbeke, M. Verderi, B.L. Wendt, H. Wenzel, D.H. Wright, D.M. Wright, T. Yamashita, J. Yarba, H. Yoshida, Recent developments in Geant4, Nucl. Instrum. Methods Phys. Res. A 835 (2016) 186–225, http://dx.doi.org/10.1016/J.NIMA.2016.06.125.

[36] Eljen technology, 2022, https://eljentechnology.com/products/plastic-scintillators.

[37] ONSEMI, 2022, https://www.onsemi.com/.

[38] C. Neacsu, R. Lica, G. Pascovici, C. Mihai, S. Rothe, A miniaturized low-power SiPM-based β detector for the ISOLDE Fast Tapestation, Nucl. Instrum. Methods Phys. Res. A 1026 (2022) 166213, http://dx.doi.org/10.1016/J.NIMA.2021.166213.

[39] C. Marquet, et al., High energy resolution electron beam spectrometer in the MeV range, JINST 10 (2015) P09008, http://dx.doi.org/10.1088/1748-0221/10/09/P09008.

[40] FASTER, 2022, http://faster.in2p3.fr/index.php/about-faster.

[41] F. Cresto, et al., 2023, in preparation.